Research Article Vol. 11, No. 2 / 1 February 2020 / Biomedical Optics Express 735

Biomedical Optics EXPRESS

Comparing strategies for deep astigmatism-based single-molecule localization microscopy

Marijn Siemons, Bas M. C. Cloin, Desiree M. Salas, Wilco Nijenhuis, Eugene A. Katrukha, and Lukas C. Kapitein*

Cell Biology, Neurobiology and Biophysics, Department of Biology, Faculty of Science, Utrecht University, Padualaan 8, 3584 CH Utrecht, The Netherlands

*l.kapitein@uu.nl

Abstract: Single-molecule localization microscopy (SMLM) enables fluorescent microscopy with nanometric resolution. While localizing molecules close to the coverslip is relatively straightforward using high numerical aperture (NA) oil immersion (OI) objectives, optical aberrations impede SMLM deeper in watery samples. Adaptive optics (AO) with a deformable mirror (DM) can be used to correct such aberrations and to induce precise levels of astigmatism to encode the z-position of molecules. Alternatively, the use of water immersion (WI) objectives might be sufficient to limit the most dominant aberrations. Here we compare SMLM at various depths using either WI or OI with or without AO. In addition, we compare the performance of a cylindrical lens and a DM for astigmatism-based z-encoding. We find that OI combined with adaptive optics improves localization precision beyond the performance of WI-based imaging and enables deep (>10 µm) 3D localization.

1. Introduction

In Single-Molecule Localization Microscopy (SMLM) the diffraction limit is circumvented by analyzing the Point Spread-Function (PSF) of single fluorescent molecules to obtain precise information about the molecule's position in x and y [1,2]. Subsequent localization of large numbers of fluorophores provides structural information with a resolution in the order of nanometers [3]. A common way to determine the z-position of fluorophores is by inducing astigmatism in the detection path, either by introducing a cylindrical lens (CL) [4] or an adaptive optical element [5]. Inducing astigmatism creates slightly separate focal planes for the x- and y-direction, with the average focal plane (AFP) situated halfway in between them. The PSF of a fluorophore positioned in the AFP appears round, while the PSFs of fluorophores outside AFP appear elliptical. The orientation of the major and minor axis of an elliptical PSF indicates whether a fluorophore is positioned above or below the AFP and the distance to the AFP can be determined from the amount of ellipticity.

When imaging deeper into a sample, aberrations induced by both the optical setup and the sample distort the PSF and will decrease the localization precision [6,7]. Sources of setup-induced aberrations are for instance imperfections in the objective, other lenses and dichroic mirrors. High NA oil immersion (OI) objectives, often used for SMLM, provide optimal imaging close to the coverslip, but focusing deeper into a water-based sample results in large, mainly spherical aberrations because of the mismatch in refractive index between the immersion oil (~1.52) and the sample (~1.33). The use of water immersion (WI) objectives limits this mismatch at the expense of a lower NA and, as a result, lower photon counts and a decreased resolution [8]. Deeper imaging also increases the distance light has to travel through the sample, increasing scattering and refraction of the fluorescence emission due to inhomogeneities in the sample [7].

#382023 https://doi.org/10.1364/BOE.382023
Journal © 2020 Received 30 Oct 2019; revised 12 Dec 2019; accepted 13 Dec 2019; published 10 Jan 2020

Biomedical Optics EXPRESS

Aberrations induced by both setup and sample can be corrected using an adaptive optical element, such as a liquid crystal-based spatial light modulator (SLM) or a deformable mirror (DM) [9]. In SMLM applications, DMs are preferred because they reflect >95% of the incoming light and are not sensitive to the polarization of the light, implying less photon loss compared to SLMs. Since in SMLM the excitation pattern is not critical, implementing a DM in the detection path only is sufficient. In addition, a DM can also be used to induce a tunable amount of astigmatism for 3D-SMLM [5]. Previous work has shown that correction of system-induced aberrations and the simultaneous induction of astigmatism using a DM can result in high-quality 3D-SMLM images of structures close to the coverslip [5]. Additionally, it was shown that the amount of induced astigmatism influences the x-, y- and z-precision [10], but the settings for optimal x-, y-, and z-resolution have not been systematically explored.

Correction of setup- and sample-induced aberrations becomes more important when imaging deeper into a sample, especially when using an OI objective. At a depth of 6 µm in cultured COS-7 cells, correction of aberrations resulted in improved 2D and 3D-SMLM as measured in amount of localizations and degree of structure reconstruction [9]. Despite this evidence that DM-based adaptive optics can improve 2D- and 3D-SMLM when imaging deeper into a biological sample, a thorough investigation of the effect of aberration correction on SMLM performance as function of imaging depth is lacking. Furthermore it has been reported that with OI the astigmatic z-encoding is impaired due to the refractive index mismatch [11–13]. It is unclear whether the use of an OI objective in combination with AO outperforms a WI objective where there is very little or no refractive index mismatch. Lastly, a comparison of astigmatism-based 3D-SMLM using either AO or a CL as function of imaging depth has not been reported.

Here we first explored how localization precision as a function of imaging depth in 2D-SMLM is affected by DM-based aberration correction in combination with an OI objective. These results were compared with the performance of a 60x WI objective without active aberration correction. Secondly, astigmatism-based PSF z-encoding as a function of imaging depth was compared between a CL and a DM and the field distortion and astigmatic field dependency were assessed for both techniques. Thirdly, we experimentally addressed the optimal value of induced astigmatism to achieve the highest x-, y-, and z-localization precisions and compared this to the theoretical optimum. Finally, we performed 3D-SMLM using a DM to correct aberrations and induce astigmatism and succeeded in super-resolved imaging at high imaging depth in a biological sample.

2. Materials and methods

2.1. Microscopy

SMLM microscopy was performed on a Nikon Ti-E microscope equipped with a 100x Apo TIRF OI objective (NA. 1.49), a 60x Plan Apo IR WI objective (NA 1.27), and Perfect Focus System 3 as shown in Fig. 1(a). Excitation was achieved with a mercury lamp or via a custom illumination pathway with a Lighthub-6 (Omicron) containing a 638 nm laser (BrixX 500 mW multimode, Omicron), a 488nm laser (Luxx 200 mW, Omicron), and a 405 nm laser (Luxx 60 mW, Omicron). Emission light was separated from excitation light with a quad-band polychroic mirror (ZT405/488/561/640rpc, Chroma), a quad-band emission filter (ZET405/488/561/640m, Chroma), and an additional single-band emission filter (ET525/50m for green emission and ET655lp for far-red emission, Chroma). Fluorescence was detected via either a pathway containing a removable Nikon CL (left port), or a pathway containing the MicAO 3D adaptive optics system (right port, Imagine Optic, France, www.imagine-optic.com). The latter pathway uses a relay system of two lenses (L2 and L3) with equal focal length ($f = 500$ mm) to relay the image plane onto the sCMOS camera (Hamamatsu Flash 4.0v2). A third lens ($f = 750$mm, L1) was placed in the intermediate image plane (IIP), which together with the tube lens and L2,

Biomedical Optics EXPRESS

conjugate the back focal plane of the objective to a DM (MIRAO 52-e, Imagine Optic). L1 is required because the objective and tube lens inside the microscope body are placed too close to each other (by approximately 5 cm) to form a true 4F system. Without this lens in the IIP the DM would not be properly conjugated to the pupil plane. A removable mirror (M3) was used to optionally deflect the light to a Shack-Hartmann wave-front sensor (HASO3, Imagine Optic).

Table 1. Number of experimental repeats and molecules used in Fig. 1.

	OI without AO	
depth (µm)	N	n (sum of N acquisition)
0	3	32497
4.4	3	118441
8.8	3	37805
17.6	3	37805
25.5	3	22870
	OI with AO	
depth (µm)	N	n (sum of N acquisition)
0	3	41294
4.4	3	74233
8.8	3	48012
17.6	2	61730
25.5	3	91253
	WI	
depth (µm)	N	n (sum of N acquisition)
0	1	29809
5	3	43961
10	3	45739
20	3	21119
30	3	41546

The back focal plane of the objective is imaged with a diameter of $2NAf_{L2}/M$ onto the DM, with M being the magnification of the objective. For the 100x oil and 60x water immersion objectives, this results in 14.9 mm and 21.2 mm, respectively. The size of DM (15 mm) is therefore ideal in combination with the oil immersion objective, but is incompatible with the water immersion objective as the DM would clip the beam of the collected fluorescence. Therefore all experiments with the water immersion objective are performed on the non-corrected left port.

The camera had an effective pixel size of 65 nm (100x objective) or 108 nm (60x objective) and the camera output was converted to photons using the calibration factor supplied by the manufacturer. Samples were positioned in the *x*- and y-direction with an M-687 PILine stage (PI) and in the *z*-direction with either the Perfect Focus System or a P-736 PInano stage (PI). The DM and wave-front sensor were controlled by Imagine Optic software, all other components by Micromanager [14]. Aberrations were corrected using the image-based 3N algorithm [15] as implemented in the Imagine Optic software, with maximum contrast as optimization metric. In short, per Zernike mode three images of a 100 nm fluorescent bead were acquired with a zero, negative, and positive amplitude bias of that Zernike mode applied to the DM. The optimization metric is measured in the three images and a second-order polynomial fit is used to determine the amount of applied Zernike mode corresponding to the maximum of the metric. This is done per Zernike mode, and the sum of Zernike modes with corresponding amplitudes is subsequently

Biomedical Optics EXPRESS

applied to the mirror to correct aberrations. The amplitude of the Zernike coefficients are reported in nm of root mean square (RMS) normalized Zernike modes [16]. This RMS unit describes the RMS displacement of the mirror surface with respect to a flat surface, integrated over the whole mirror.

For SMLM, the sample was continuously illuminated with 638 nm light. In addition, the sample was illuminated with 405 nm light at increasing intensity to keep the number of fluorophores in the fluorescent state constant. Typically 5,000 frames for *in vitro* microtubules and 10,000 frames for Caco2-cells were recorded per acquisition with exposure times of 30–40 ms.

2.2. Collection efficiency correction for comparing water and oil immersion objectives

The WI and OI objectives have different magnifications, a different NA and a different transmission efficiency. This results in different excitation intensities as well as different collection efficiencies, which both affect the localization precision. In order to compensate for these differences, we aimed to compare the localization precisions of both objectives given a similar number of emitted photons. First, we calculated a transmission correction for the collected number of photons, which included the transmission of the objectives, the reflectance at the cover glass, and the transmission/reflection efficiencies of the CL or AO-module.

First, we address the transmission at the cover glass, for which two factors are important: The Fresnel coefficients at the medium/coverslip interface and the coverslip/immersion interface and the NA of the objective lens. The energy transmission for randomly polarized light at an interface 1→2 is given by [17]

$$T_{1\to 2} = \frac{1}{2}\frac{n_2\cos(\theta_2)}{n_1\cos(\theta_1)}\left[\left(\frac{2n_1\cos(\theta_1)}{n_2\cos(\theta_2)+n_1\cos(\theta_1)}\right)^2+\left(\frac{2n_2\cos(\theta_1)}{n_1\cos(\theta_2)+n_2\cos(\theta_1)}\right)^2\right], \tag{1.1}$$

with n_1 and n_2 the refractive indices on either side of the interface and θ_1 and θ_2 the respective angles of the light with respect to the interface. The first term is due to wave-front compression and the second term contains the Fresnel coefficients for S- and P-polarized light. From this equation, the ratio of the collection efficiency for a point emitter of the OI and WI objective can be calculated as

$$\frac{CE_{oi}}{CE_{wi}} = \frac{\int_{\phi=0}^{2\pi}\int_{\theta=0}^{\theta_{1.329}} T_{water\to glass}\sin(\theta)d\theta d\phi}{\int_{\phi=0}^{2\pi}\int_{\theta=0}^{\theta_{1.27}} T_{water\to glass}T_{glass\to water}\sin(\theta)d\theta d\phi}, \tag{1.2}$$

with $\theta_{1.329}$ and $\theta_{1.27}$ the angles corresponding a NA of 1.329 (88°) and 1.27 (73°) and where we assumed there is no refractive index mismatch between the glass and oil. The largest angle the OI objective collects light is 1.33, as deeper than 1 µm the super-critical angle fluorescence (SAF) can be ignored. In practice this effective NA is slightly reduced as the 90° collection angle can only be achieved at the coverslip. We estimated from the working distance and the size of the front lens that at a depth of 30 µm the largest collection angle is 88°, corresponding to a NA of 1.329. This calculation revealed that the CE of the OI objective lens is 129% the efficiency of the WI objective. This is slightly less than if one would only consider the solid angle and ignore the Fresnel coefficients: (1-cos($\theta_{1.329}$)) / (1-cos($\theta_{1.27}$)) = 137%.

The transmission efficiencies of the objectives itself are listed as 83% (WI) and 78% (OI) in their specifications for light with a wavelength of 690 nm. Lastly, we estimate the transmission of the CL and AO-module, where we assumed all optics have the appropriate coating (99.5% transmission/reflection per interface) and are not damaged. Based on two interfaces, the CL-module has an estimated transmission of 98% when in bypass mode. The AO-module consists of 3 lenses and 4 broadband mirrors. The DM itself has a silver coating with a reflectance of 98% at 15 degree incidence. These results in a total transmission of 93% for the AO-module.

Biomedical Optics EXPRESS

All these efficiencies add up to a total efficiencies of 82% for WI + CL and 95% for OI + AO compared to OI + CL. As expected OI collects significantly more light compared to WI, but the loss in the AO-module should be taken into account as well. These efficiency factors enabled us to compare the achieved localization precision between the different strategies, OI + CL, WI + CL and OI + AO, in a consistent manner.

2.3. In vitro imaging of fluorescent beads and microtubules

To assess the performance of WI and OI immersion as function depth (Fig. 1) we used a sample which consisted of labeled microtubules and beads suspended in agarose. These HiLyte Fluor 647 labeled microtubules (MTs) were prepared from stabilized seeds as described earlier [18] and stored at −80°C. HiLyte Fluor 647 (HF647)-tubulin was purchased from Cytoskeleton. Before sample preparation seeds were kept at 37°C for 2–4 h and stabilized by 1% glutaraldehyde. Agarose gel was prepared by adding 4% agarose (A9539, Sigma Aldrich) to 100 mM Tris at pH 8. MT seeds and 100 nm green fluorescent beads (final dilution 1/2000; F8803, ThermoFisher) were added to heated agarose, gently mixed, and put on a microscope slide between two pieces of double sided tape. For SMLM, mercaptoethylamine and an oxygen scavenging system consisting of glucose, glucose oxidase and catalase were additionally added to the heated agarose (final concentrations: 50 mM MEA, 5% w/v glucose, 560 µg/ml glucose oxidase, 40 µg/ml catalase). A coverslip was pressed onto the tape and the sample was cooled under running water to quickly solidify the agarose.

When focusing into a water-based sample with an OI objective, the imaging depth has to be corrected for the refractive index mismatch. The imaging depths for data obtained with the OI objective are reported as 0.93 n_{water}/n_{oil} z_{stage} where the factor 0.93 is obtained from simulations with a PSF model similar to [19].

Single molecule localization precisions at z-stage positions of 0, 5, 10, 20 and 30 were determined using the previously described ImageJ plugin Detection of Molecules (DoM, available at https://github.com/ekatrukha/DoM_Utrecht) [20]. The detection size of the PSF was set to 110% of the ideal PSF (λ/2NA) and spots where the width deviated more than 30% from the detection size where disregarded as false positives. The total localization precision was calculated as $\sigma_{tot} = \sqrt{\sigma_x{}^2 + \sigma_y{}^2}$. In all cases, the reported localization precisions (or errors of other fitting parameters θ) were estimated using the covariance matrix C of the least-squared fitting

$$\sigma_{\theta_k}^2 = \frac{\chi^2}{n-p} C_{kk}, \tag{1.3}$$

with χ^2 the chi-squared value, n the number of data points (pixels) and p the number of fit-parameters. Localizations with an uncertainty above 50 nm were discarded. Mean localization precision were calculated from three acquisitions per depth.

2.4. Comparison of 3D calibration curves

Calibration curves (Fig. 2) were obtained by making z-stacks with 20 nm steps of 100 nm green fluorescent beads suspended in the agarose gel. For each z-step, the x-width and y-width of the PSF (as determined from a Gaussian fit using DoM) were subtracted and plotted against the z-position. PSF x- and y-width was taken as the full width half maximum (FWHM) value, equal to $2\sqrt{2\,ln\,2}$ of the Gaussian's standard deviation (spread). Calibration curves were measured at imaging depths of 0.0, 0.8, 3.2, 8.1, and 16.2 µm (OI) and 0.0, 5.0, 10, 15, and 20 µm (WI). Astigmatism was induced with the CL or the DM. The amount of astigmatism induced with the DM was increased with increasing imaging depth, from 60 nm RMS at the coverslip to 120 nm RMS at a depth of 16.2 µm, to obtain similar calibration curves.

Biomedical Optics EXPRESS

Simulations of PSFs at different depths for OI with and without AO (Fig. 3) were performed with a vectorial PSF model [21,22]. This model implements the effect of the high NA and includes the NA, pixel size, wavelength, refractive indices of the immersion oil, the cover glass and the surrounding medium of the bead, the distance from the bead to the cover glass and the size of the bead.

2.5. Comparison of field-of-view distortion

The distortion of the field of view (Fig. 4) was assessed by taking an image of beads within the field of view of the camera with and without astigmatism using the CL, and at another position using AO (0 and 60 nm RMS astigmatism). To prepare the bead sample, a small sample volume was created by attaching a coverslip to a microscope slide using double-sided tape. 100 nm green fluorescent beads were diluted in PBS (1/100,000) and incubated for 10 minutes in the sample volume to allow nonspecific adsorption. Free beads were then washed away with PBS and the volume sealed with vacuum grease. To assess the distortion of the field-of-view, a custom MATLAB-script was used that for each particle in the image without astigmatism finds the highest-intensity particle in the image with astigmatism within a certain area around the first. Based on a first assessment of positional shift, this area was set to be an ellipse with longer y-axis to account for the mostly y-shifted positions. Ellipse radii of 0.67 pixels in x and 6.7 pixels in y were used for CL images, and of 1.0 pixels in x and 3.2 pixels in y for AO images. First, the global translation was determined and subtracted from the individual shifts to account for non-ideal alignment. Then, the leftover positional shifts were decomposed in the x- and the y-direction. To produce the graph in Fig. 4(d), shifts in the y-direction were averaged over particles with positions within a 50 pixel windows in the y-direction in the images without astigmatism. After removal of shifts more than 2 times the standard deviation from the mean, the mean and standard deviation were recalculated to produce the graph in Fig. 4(d). In total 522 and 501 shifts were used for CL and AO, respectively.

2.6. Comparison of field-dependent aberrations

The field-dependency of the aberrations and induced astigmatism (Fig. 5) was assessed by taking a through focus scan (TFS) of a bead and performing a phase-retrieval algorithm on this TFS [22]. The bead was then moved in a 11×11 grid over a 32×32 µm field of view, taking a TFS at each point. The phase retrieval algorithm fits Zernike coefficients up the sixth radial order $Z_6^{\pm 6}$ (23 orders in total). This was performed for the OI lens either on the left port with and without CL and for the right port with AO (0 and 100 nm RMS astigmatism).

2.7. Tuning of astigmatism

For Fig. 6, samples with green fluorescent beads on a coverslip were prepared as described above, with a bead dilution of 1/50,000. Z-stacks were made with 50 nm steps with an astigmatism that varied between 10 and 100 nm RMS with steps of 10 nm, induced with the DM. PSF widths were determined using DoM. The offset between the x-focal plane and the y-focal plane was determined from 3rd order polynomial fits to the bottom part (x- and y-width < 8 pixels) of the curves of x- and y-width as function of the z-position of the stage. The focal plane offset was calculated by dividing the difference in z-position between the minima of the two fits by two. The focal plane offset was determined for different amounts of induced astigmatism and for each setting a linear fit to the z-position of the stage versus the difference between x-width and y-width resulted in a slope α, which was used to calculate the z-position of localized particles based on their PSF widths. The uncertainties in the z-position were calculated using error propagation:

$$\sigma_z = \sqrt{\alpha^2(\sigma^2_{x-\text{width}} + \sigma^2_{y-\text{width}})}, \tag{1.4}$$

Biomedical Optics EXPRESS

where α is the slope of the calibration curve and $\sigma_{x/\mathrm{y-width}}$ the error in determining the x- and y-widths, as determined from the Gaussian fits.

2.8. Experimental localization precision and calculation of Cramér-Rao lower bound

The experimental localization precision in Fig. 6 was measured by acquiring 25 frames of a fluorescent bead at a certain z-position. The standard deviation of the estimated position is a measure of the achieved localization precision, assuming there is no drift during the 25 frames. To achieve a signal to noise ratio representative for a single molecule the camera integration time and the bright-field illumination were tuned to achieve around 50 background photons per pixel and 8000 signal photons.

The Cramér-Rao Lower Bound (CRLB) was obtained from the vectorial PSF model described above, which incorporates shot noise and Gaussian read noise from the CMOS camera. The required background photon levels for the CRLB computation were estimated from the estimated background level by DoM. To estimate the signal photon count, we used a through-focus scan with 100 ms exposure time, followed by phase retrieval. The relevant signal photon count was then calculated as the ratio of the experimental (3 ms) and through-focus exposure time (100 ms).

2.9. SMLM imaging of Caco2-BBE cells

For Fig. 7, SMLM was performed on Caco2-BBE cells (a gift from S.C.D. van IJzendoorn, University Medical Center Groningen, The Netherlands). These cells were maintained in DMEM supplemented with 9% FBS, 50 µg/µl penicillin/streptomycin and 2 mM L-glutamine. For immunofluorescent imaging, cells were seeded on 18 mm coverslips at a density of $1 \times 10^5/\mathrm{cm}^2$ and cultured for 10–12 days to allow for spontaneous polarization and brush border formation. Cells were fixed with 4% paraformaldehyde in PBS for 10 min, washed with PBS, permeabilized with 0.5% Triton *X*-100 in PBS for 15 min and blocked with 3% BSA in PBS for at least 1 h. Cells were incubated with primary antibodies, either Mouse-anti-Ezrin (610602; BD Biosciences; 1 µg/ml) or Mouse-anti-Villin (610358; BD Biosciences; 1 µg/ml), for 6 h at room temperature, washed with PBS, incubated with secondary antibodies, Goat-anti-mouse Alexa 647 (A21236; Life Technologies; 6.7 µg/ml), for an additional hour at room temperature and washed with PBS. SMLM imaging was performed in the same buffer as the SMLM imaging of *in-vitro* MTs.

3. Results and discussions

To examine the effect of a DM on localization precision in OI-based single-molecule localization microscopy, we embedded HF647-labeled microtubules and fluorescent beads in an agarose gel. After optimizing the DM shape using the fluorescent beads before each acquisition, we compared localization precision with and without adaptive optics at imaging depth between 0–30 µm. In addition, we used a WI objective to measure localization precision in the absence of a refractive index mismatch.

When using WI, we found only a minor decrease in localization precision in the histogram of localization precisions when imaging deeper into the sample, indicating that the imaging quality was not or only slightly degraded (Fig. 1(b)). We attributed this slight decrease in localization precision to a small refractive index mismatch between the water immersion and the sample. In contrast, with OI the localization precision strongly degraded when imaging deeper (Fig. 1(c)). Close to the cover slip, localization precision was better than with WI, likely due to the super-critical angle fluorescence which is captured by the high NA objective. When we used AO, the loss in localization precision at greater depth was prevented to a high degree (Fig. 1(d)). Often in reconstructing SMLM images localizations with a precision above a certain threshold are discarded, which makes the fraction of localizations below this threshold an important parameter for achieving proper reconstructions. Figure 1(e) shows that the fraction of localizations with a precision below 15 nm does not decreases significantly for the WI or OI with adaptive optics, but

Biomedical Optics EXPRESS

decreases rapidly without correction for the OI. Moreover, AO improves the average localization precision by a factor of 1.3 at a depth of 26 µm and doubles the fraction of localizations below 15 nm (Fig. 1(f)). This increase in localization precision is mostly due to the differences in PSF shape, rather than a strong increase in detected photons, because even for events with the same amount of estimated photons the localization precision with correction is highly improved (Fig. 1(g)).

Because WI has a lower collection efficiency than OI + AO (see methods), we compared the localization precision for fluorophores for which the emitted photons were estimated to be similar. That is, fluorophores detected with OI with photon counts between 1400–1600 per frame were compared with fluorophores in the range of 1331–1522 and 1155–1320 for OI + AO and WI, respectively (Fig. 1(g)). This analysis revealed that WI outperformed OI, while OI + AO outperformed WI in achieved localization precision for the same amount of estimated emitted photons. For the photon counts mentioned above, the fraction of localizations with an estimated precision below 15 nm was 56% for WI, 47% for OI and 77% for OI + AO. Moreover, the median of localization precision was reduced by 17% (14.5 nm for WI and 12.0 nm for OI + AO). This reduction is more than what would be expected based on the higher collection efficiency of the OI objective ($1 - \sqrt{95/82} = 7\%$). The additional improvement is likely due to the difference in pixel size and a small amount of spherical aberration that is introduced when imaging with WI. Thus, OI + AO outperforms WI when imaging deep into watery samples.

Next, we compared the use of either a CL or a DM to induce astigmatism for z-localization at different imaging depth. When using OI, the PSF of fluorescent beads close to the coverslip (depth < 5 µm) showed clear ellipticity after insertion of the CL. At larger imaging depth, however, the PSF remained largely symmetric and could not be used to encode the z-position (Fig. 2(a)). This is reflected in the calibration curves obtained by plotting the difference in PSF width in the x and y direction as a function of z-position (Fig. 2(b)).

Similarly, even after optimizing the DM to correct for the first order spherical aberration, the degree of astigmatism sufficient for z-encoding near the coverslip did not induce strong ellipticity at larger imaging depth. Nevertheless, more astigmatism could easily be added, resulting in consistent ellipticity and corresponding calibration curves at depths up to 18 µm (Fig. 2(c) and 2(d)). When the WI objective was used in combination with the cylindrical length, the induced ellipticity was less pronounced (Fig. 2(c)). Although the calibration curve appears similar to the ones obtained with OI and remains unaltered for depths from 0–20 µm (Fig. 2(f)), the PSF for the WI with cylindrical lens was not well represented by a 2D Gaussian. This indicates that this specific cylindrical lens is not a suitable for this WI objective.

The requirement for increased levels of astigmatism for z-encoding at increased depth with OI objectives has been reported previously [13], but the origins of this effect had remained unclear. To investigate this, we performed simulations to simulate PSFs at different depths for OI with and without AO (Fig. 3). We placed an emitter at 15 µm from the coverslip and performed AO by simulating a 3N correction algorithm to correct primary spherical aberration (Z_4^0). As correcting spherical aberration results in a focus shift, the primary spherical aberration was corrected iteratively by 3N correction and refocusing by stage movement until convergence (similar to the experiments). After correction of the primary spherical aberration astigmatism was added and a PSF is computed. The amount of astigmatism was then optimized to regain a calibration curve with the same slope as the curve obtained at the coverslip (Fig. 3(a)).

The simulated PSFs at the coverslip and at a depth of 15 µm were qualitatively strikingly similar to the experimental ones (Fig. 3(b)). Inspection of the corresponding wave-fronts revealed that, at a depth of 15 µm, the applied astigmatism is 'drowned' in the spherical aberration caused by the refractive index mismatch. However, even with AO to correct the first-order spherical aberration, applying 60 nm of astigmatism did not result in the required ellipticity (Fig. 3(e)). This was caused by the significant amount of higher-order spherical aberrations (Z_6^0, Z_8^0, etc.), as

Biomedical Optics EXPRESS

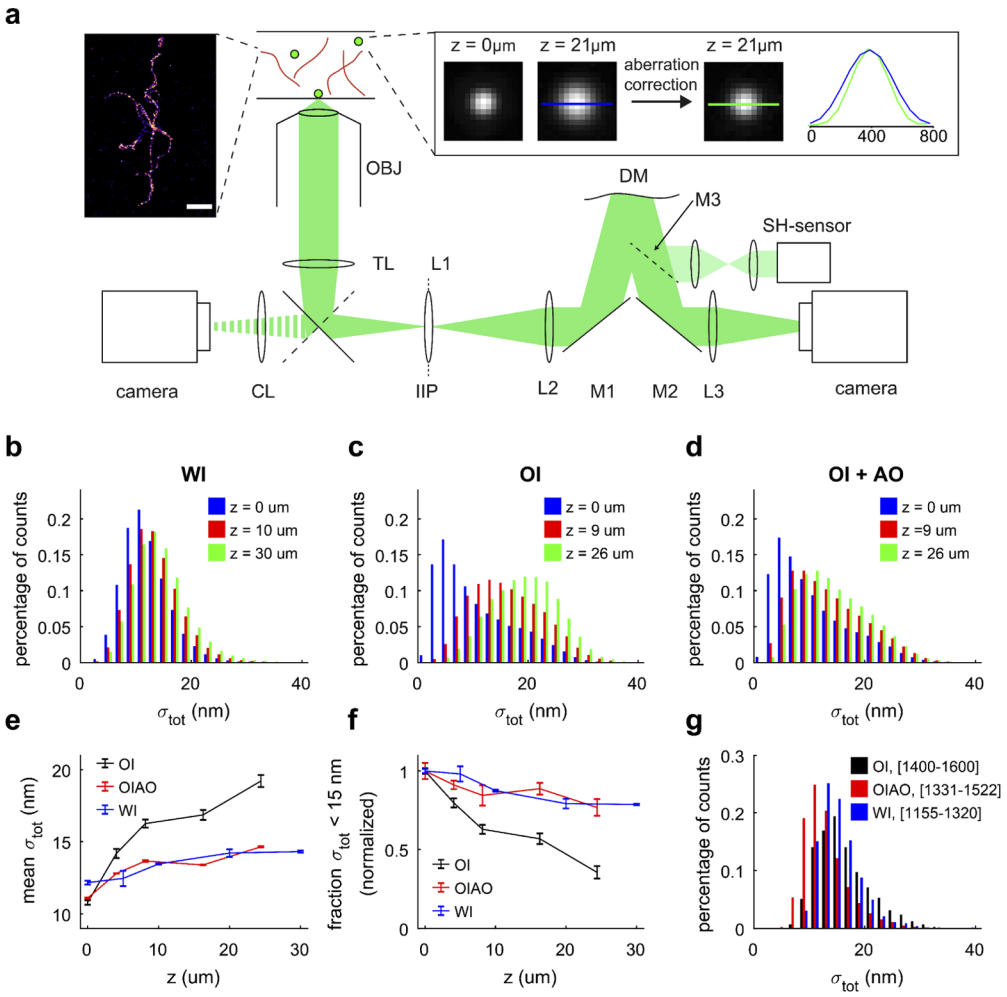

Fig. 1. Use of Adaptive optics improves 2D SMLM away from the coverslip. (a) Schematic representation of the imaging setup. Fluorescence from the sample, consisting of green fluorescent beads and stabilized HiLyte647-conjugated microtubules suspended in agarose gel, is collected via a water immersion (WI) or oil immersion (OI) objective and projected on a camera either directly (left side; optionally through a CL) or via a DM (two mirrors in the AO-module are not shown). Left inset shows a representative SMLM reconstruction of the HiLyte647-MTs, scalebar is 1 μm. Right inset shows images and cross sections of a fluorescent bead at the coverslip (left panel) and at 25 μm depth without (middle panel) and with aberration correction (right panel). Cross sections at the drawn lines are shown on the right. Abbreviations: OBJ: objective; TL: tube lens; IIP: intermediate image plane, M1/2/3: mirrors discussed in main text, M3 is a flip-mirror; L1/2/3: lenses discussed in main text; SH-sensor: Shack-Hartmann sensor; DM: deformable mirror. (b,c,d) Localization distribution for different imaging depths for the WI objective lens (b), OI (c) and OI with adaptive optics (d). (e) The normalized fraction of estimated localization precisions below 15 nm as function of depth. (f) The average estimated localization precision as function of depth for WI and OI with and without adaptive optics. (g) Histogram of localization precision for integrated photons counts between 1400 and 1600. This interval is corrected for transmission efficiencies of the WI objective and the AO-module. Data collection parameters are indicated in Table 1.

Biomedical Optics EXPRESS

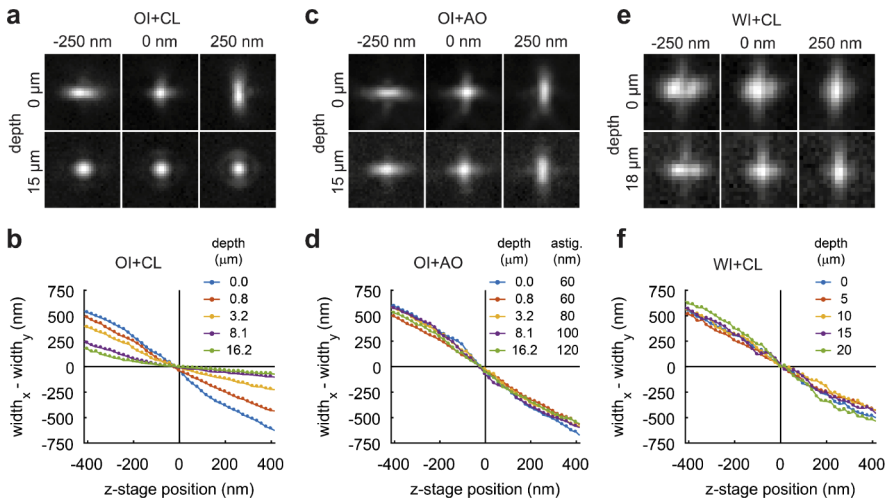

Fig. 2. Adaptive optics allow z-encoding away from the coverslip. (a) PSF with astigmatism of a 100 nm green fluorescent bead in agarose gel on the coverslip (top panels) and at 18 µm depth (bottom panels) at stage z-positions of −250 nm (left), 0 nm (middle) and 250 nm (right panel) with respect to the focal plane of the OI objective. Astigmatism was induced with the CL. (b) Curves of the difference between PSF x-width and y-width as function of the stage z-position with respect to the objective focal plane, at increasing distance from the coverslip for the 100x OI objective. (c,d) Same as (a) and (b) but adaptive optics was used to both correct aberrations and induce astigmatism. (e,f) Same as A and B, but imaged with the 60x WI objective. The size of the ROI is 2×2 µm in all images.

the wave-front was still significantly aberrated at the edge of the pupil. Similar to the experimental results (Fig. 2(b)), we could obtain the desired calibration curve by introducing more astigmatism (Fig. 3(d) and 3(e)).

The optimal amount of astigmatism obtained from the simulations deviated slightly from the amount of astigmatism that was required experimentally (Fig. 3(f)). We found that the theoretical amount of astigmatism was dependent on the (calibration) NA. When calibrating the DM with a Shack-Hartman sensor it is likely that the spots at the edge of the pupil are not detected, which effectively reduces the calibration NA. We therefore repeated our simulation with an NA of 1.43 instead of 1.49, which corresponds to a calibration in which per row/column one spot is not detected by the Shack-Hartmann sensor. It is worth noting that the effective NA (the maximum angle at which fluorescence is collected) is 1.33 in both cases due to the refractive index mismatch. The calibration NA only determines the pupil-size at which the Zernike modes are defined and normalized.

The predicted amount of astigmatism for a calibration NA of 1.43 matches well with the experiments (Fig. 3(f)). The remaining discrepancy near the coverslip is likely due to hysteresis in the mirror or suboptimal correction of primary spherical aberration. Altogether, these results demonstrate that the remaining, non-corrected higher-order spherical aberrations are the major reason for the loss in ellipticity when imaging deeper into a watery sample with a constant amount of astigmatism applied.

When using the CL, we noted that its insertion into the optical path induced a deformation of the image in one direction (Fig. 4(a)). To quantify this, we imaged fluorescent particles immobilized on the coverslip and measured how the position of their imaged altered upon insertion of the lens. This revealed a lateral displacement that increased linearly with the distance from the center of the field of view, consistent with a decrease in magnification of 3.6% (Fig. 4(b)–4(d)). In

Biomedical Optics EXPRESS

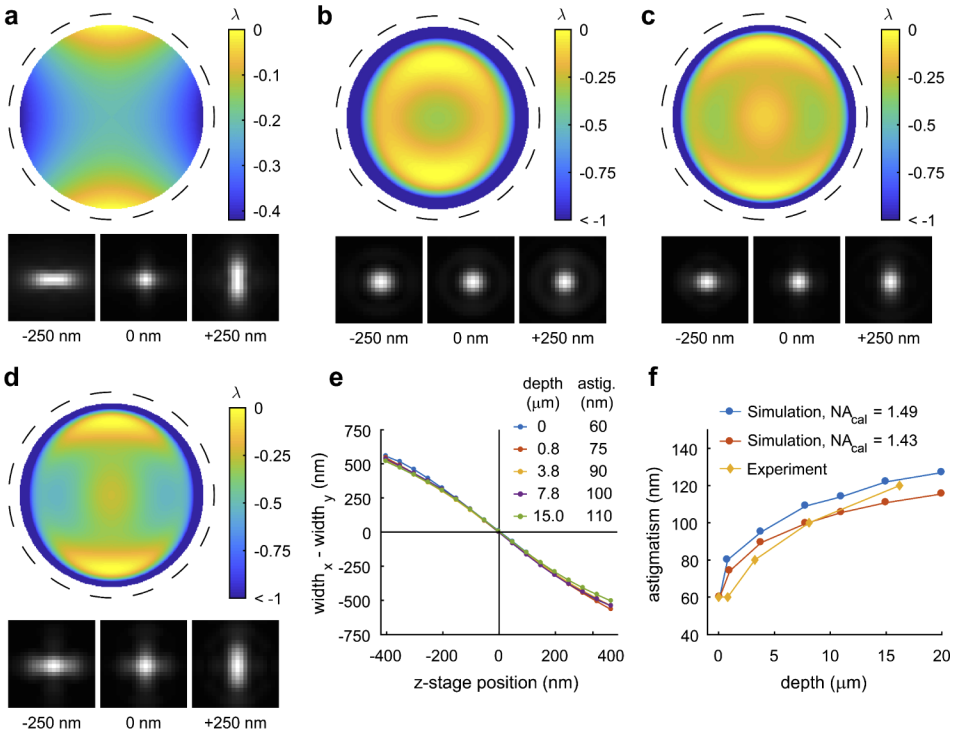

Fig. 3. Simulation study on the depth-dependent loss of astigmatism. a) Aberration profile with 60 nm astigmatism at the coverslip and corresponding PSF at different z-positions. The dashed line indicates the NA of the objective (1.49). b) The aberration profile without AO with 60 nm astigmatism at a depth of 15 um. c) The aberration profile and corresponding PSF at a depth of 15 um with AO with 60 nm astigmatism. d) The aberration profile at a depth of 15 um with AO with 120 nm astigmatism. e) Simulated calibration curves at different depths with AO performed. In order to maintain a similar curve, more astigmatism needs to be added, even with AO. f) Optimal amount of astigmatism as function of depth for different calibration NAs and alongside the experimental values.

contrast, inducing astigmatism using the DM did not induce a change in magnification (Fig. 4(c) and 4(d)). Although the precise optical design of the CL-module has not been published, this demagnification indicates that the CL is not inserted in the pupil plane.

Next, we assessed the field dependency of the induced astigmatism by moving a bead in a 11×11 grid over the FOV, taking a through-focus scan at each position and using a phase-retrieval algorithm to estimate the aberrations and the level of induced astigmatism. This was performed either without CL/DM-induced astigmatism and with CL/DM-induced astigmatism. The size of the FOV where the aberration level is below the Maréchal's limit (<72 mλ) is comparable for both configurations (Fig. 5(a) and (d)). Strikingly, the most dominant for the CL-module (in the absence of the CL) was astigmatism (Fig. 5(b)), while first-order coma was the most predominant aberration in the AO-module (Fig. 5(e)). The latter is likely due to the two additional lenses in the 4F system. In the case of induced astigmatism, the direction of astigmatism induced by the DM was more homogeneous over the FOV compared to the CL-induced astigmatism and the level of astigmatism was also more consistent (Fig. 5(c) and 5(f)). Inhomogeneities in the amplitude as well as the direction of the astigmatism will introduce z-accuracy errors as the global lookup table (LUT) is locally inaccurate. Thus, when performing SMLM the AO-module

Biomedical Optics EXPRESS

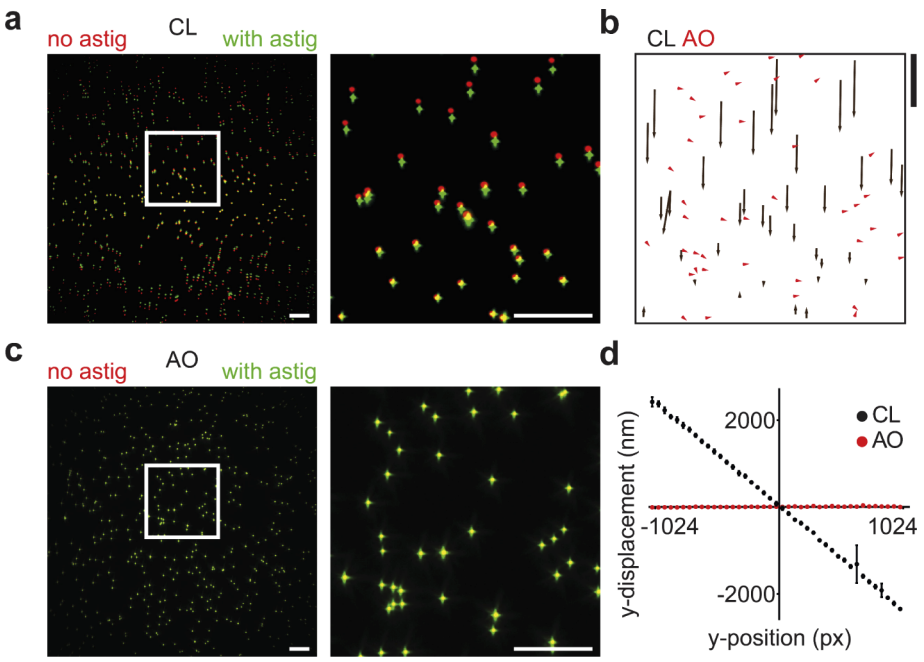

Fig. 4. Inducing astigmatism with AO does not distort the field of view. (a) Overlaid images of green fluorescent beads without (red) and with (green) CL inserted in the optical path (left) and a zoom of the region in the white box (right). Scalebar is 10 µm. (b) Displacement of bead locations when astigmatism is induced with the CL (black arrows) and with adaptive optics (red arrows). Scalebar for shifts is 1 µm. (c) Overlaid images of green fluorescent beads without (red) and with (green) astigmatism induced with the DM (left) and a zoom of the region in the white box (right). Scalebar is 10 µm. (d) Graph showing y-displacement when astigmatism is induced using the CL (black) and adaptive optics (red) as function of y-position with respect to the center of the field of view.

is expected to provide a higher degree of 3D-accuracy across a large FOV, although for optimal usage both methods would require a field-dependent lookup table [23].

Next, we wanted to explore the optimal amount of astigmatism to encode the x,y,z-location with minimal uncertainty. First, we noted that, in contrast to inducing astigmatism with a CL, deformable-mirror induced astigmatism did not alter the imaging depth at which the point spread function was symmetric. Instead, the DM shifted both the x- and y-focal points, both in opposite directions away from the initial focus (Fig. 6(a) and 6(b)). This displacement away from the original focus, called the focal plane offset, increased nearly linearly from 0 to 300 nm when increasing the astigmatism from 0 to 100 nm RMS (Fig. 6(c)). For all these different focal plane offsets, we created calibration curves that could be linearly approximated to yield a calibration slope α (nm/px) (Fig. 6(d) and 6(e)). From this and the uncertainties in the x-width and y-width obtained from fitting, we then determined the uncertainty in z as a function of the z-stage position and compared this to the CRLB and the experimentally determined localization precision (Fig. 6(f)). This revealed that the measured localization precision was optimal in the focal plane and increased away from focus. Both the least-squares standard error and the CRLB of the localization precision were below the experimentally determined localization precision, which we attributed to drift and model errors.

To examine how the z-precision depends on the amount of induced astigmatism, we determined the z-precision, averaged over a ± 250 nm z-range, for increasing amounts of astigmatism both

Biomedical Optics EXPRESS

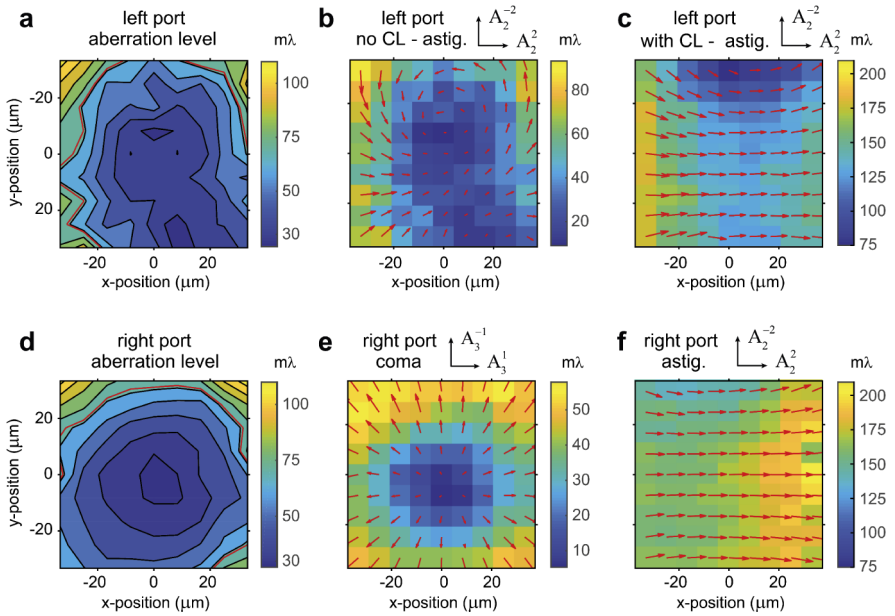

Fig. 5. Field dependency of the aberrations for the CL-module (a-c) and AO module (d-f). (a) Aberration level in the field of view for the left camera port without CL. The red line indicates Maréchal's diffraction limit (<72 mλ) . (b) The most apparent aberration in the configuration of (a) is astigmatism. Color indicates the amount of astigmatism and the arrows the direction. (c) Induced astigmatism on the left port with CL. (d) Aberration level in the field of view for the right camera port with AO-module, corrected in the center of the FOV. The red line indicates Maréchal's diffraction limit (<72 mλ). (e) The most apparent aberration in the configuration of (d) is coma. Color indicates the amount of coma and the arrow the direction. (f) Field dependency of the induced astigmatism (100 nm rms) on the right port with DM.

experimentally and using the CRLB (Fig. 6(g)). After a strong increase in precision when increasing astigmatism from 0 to 40 nm, the experimentally determined precision did not further improve, while the CRLB improved only marginally. Since increasing astigmatism will increase the PSF width, the precision in the x and y position will decrease (Fig. 6(h)). Therefore, the overall localization precision combined for x-, y- and z-direction, averaged over a $\pm$ 250 nm z-range, shows an optimum of astigmatism around 60 nm, both experimentally and theoretically (Fig. 6(j)).

Finally, we tested whether using the DM for aberration correction and astigmatism-based z-encoding would allow three-dimensional nanoscopic imaging >10 µm away from the coverslip. For this, we used the epithelial brush border of Caco2 cells, which consists of actin-rich protrusion called microvilli. Microvilli were stained using antibodies against the actin interacting protein Ezrin (Fig. 7). Importantly, using astigmatism-based z-detection we could clearly resolve tilted microvilli at a depth of around 12 µm (Fig. 7(c)). Thus, a DM in combination with a high NA OI objective enables three-dimensional nanoscopy deep in watery samples.

Biomedical Optics EXPRESS

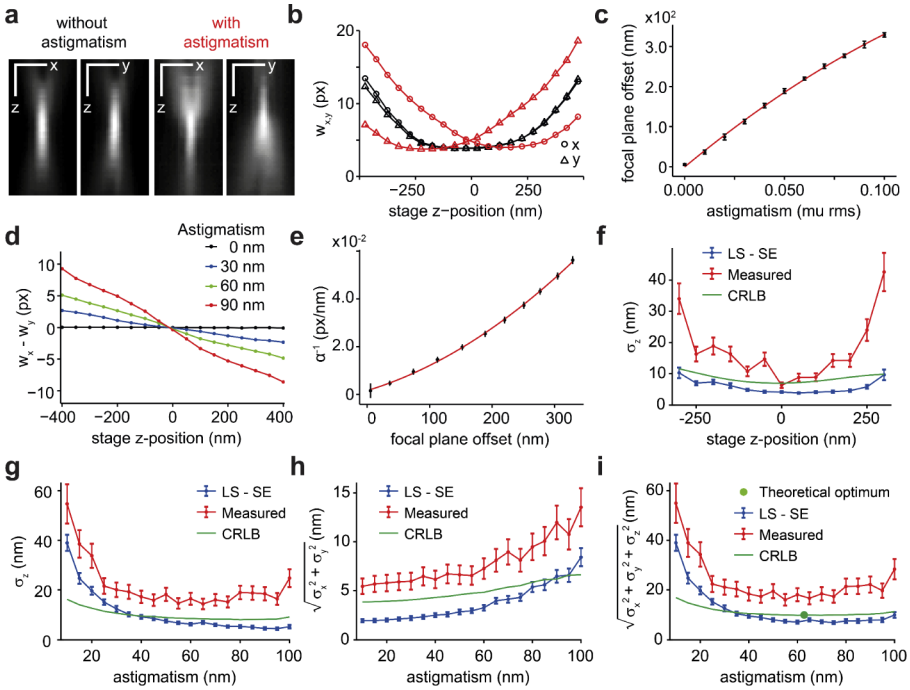

Fig. 6. Tunability of astigmatism. (a) Cross sections in x and y of a PSF of a 100 nm green fluorescent bead without astigmatism (left panels) and with 50 nm RMS astigmatism induced with the DM (right panels). Pixel size in z is 20 nm. (b) PSF width of a 100 nm green fluorescent bead in x (circles) and y (triangles) as function of the z-position of the stage, without astigmatism (black) and with 0.05 µm RMS astigmatism induced with the DM (red). (c) Focal plane offset as function of the amount of induced astigmatism (mean ± sd, N = 5 beads). Red line represents a least squares fit with a second order polynomial. (d) Difference between PSF x-width and y-width as function of the z-position of the stage for different rms astigmatism levels of 0 nm (black), 30 nm (blue), 60 nm (green), and 90 nm (red). (e) Absolute values of the inverse of calibration slope α as function of the focal plane offset (mean ± sd, N = 5). A second order polynomial was fit to the data. (f) Axial localization precision as function of z-position for the measured precision, least-squares standard error (LS-SE) and Cramer-Rao Lower Bound (CRLB) with 60 nm of astigmatism. (g) Axial localization precision as function of induced astigmatism averaged over a ± 250 nm z-range. (h) Lateral localization precision as function of induced astigmatism averaged over a ± 250 nm z-range. (i) Total localization precision as function of induced astigmatism averaged over a ± 250 nm z-range.

Biomedical Optics EXPRESS

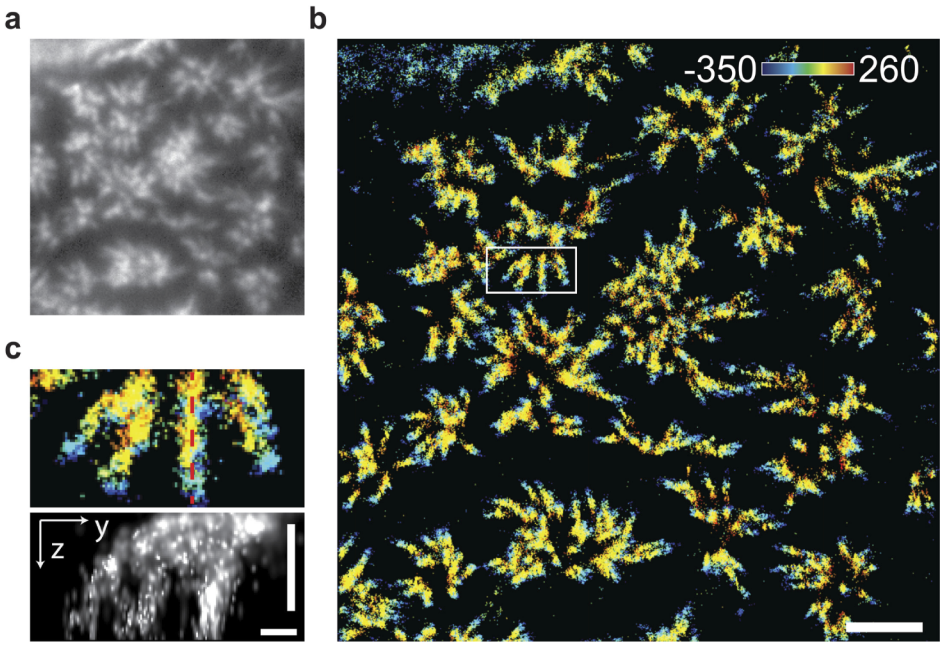

Fig. 7. Adaptive optics improves 3D SMLM using OI in Caco2-cell monolayers. (a) Widefield image of Ezrin-AF647 in a monolayer of Caco2 cells at a depth of 12 µm. (b) 3D SMLM reconstruction of (a). Scalebars is 1 µm. (c). Zoom of the area in the white box of Fig. (b) and cross section at the red dotted line (bottom panel). Scalebars are 500 nm.

4. Discussion

Here we have tested the 2D- and 3D-SMLM performance of an OI objective with and without AO as function of imaging depth and compared it to a WI objective without adaptive optics. For 2D-SMLM we found that when using OI at imaging depths above 5 µm, the use of a DM to correct aberrations improves localization precision, effectively doubling the amount of localizations with a precision below 15 nm at 24 µm depth. The achieved localization precision with WI does not degrade when imaging deeper, but when corrected for the collection efficiency, WI is outperformed by OI + AO. OI + AO results in a 21% improvement in (median) localization precision compared to WI for relevant photon levels. This improvement in localization precision does come at the expense of a more complicated and less stable optical setup that has to be optimized for every sample/acquisition.

To encode the z-position for 3D-SMLM, astigmatism was induced using either a CL or the DM. We found that using a CL in combination with an OI objective resulted in quickly deteriorating z-encoding when increasing imaging depth, which has been recently reported by others as well, but had remained unexplained [13]. Our simulations revealed that the deterioration of the z-encoding is due to leftover higher-order spherical aberration. Without the refractive index mismatch the z-encoding is maintained over large depths, as we showed using a CL in combination with WI. An advantage of the DM is that a tunable amount of astigmatism can be induced. This could be used for optimizing the amount of astigmatism for each imaging application [10]. However, we also found that there is an optimal amount of astigmatism based on the changes in x, y and z localization precisions as function of astigmatism. This suggests that a well-chosen CL combined with a WI objective could perform 3D SMLM, albeit with a reduced localization precision compared to OI with adaptive optics. Furthermore, when imaging in more

Biomedical Optics EXPRESS

inhomogeneous samples the increased importance of aberration correction might necessitate adaptive optics for optimal imaging.

Finally, we demonstrate 3D-SMLM imaging at 12 µm depth in biological samples using an OI objective with a DM. The robust DM-induced z-encoding enables discriminating microvilli lying on top of each other. Future work could explore the depth-dependent performance of other methods for achieving 3D-SMLM such as the saddle-point PSF [24] and double helix [25], which theoretically can have an isotropic localization precision. Finally, bi-plane imaging might be less sensitive to depth-induced aberration as it is less dependent on the exact shape of the PSF [26].

Funding

European Research Council (ERC Consolidator 819219); Netherlands Organisation for Scientific Research (NWO, FOM program Neurophotonics).

Acknowledgments

We thank Amol Aher for providing microtubule seeds, Sven van IJzendoorn (University Medical Center Groningen, The Netherlands) for Caco2-BBE cells and Sjoerd Stallinga (TU Delft) for helpful discussions on estimating localization uncertainties.

Disclosures

The authors declare that there are no conflicts of interest related to this article.

References

1. E. Betzig, G. H. Patterson, R. Sougrat, O. W. Lindwasser, S. Olenych, J. S. Bonifacino, M. W. Davidson, J. Lippincott-Schwartz, and H. F. Hess, "Imaging Intracellular Fluorescent Proteins at Nanometer Resolution," Science **313**(5793), 1642–1645 (2006).
2. M. J. Rust, M. Bates, and X. Zhuang, "Sub-diffraction-limit imaging by stochastic optical reconstruction microscopy (STORM)," Nat. Methods **3**(10), 793–796 (2006).
3. T. J. Gould, S. T. Hess, and J. Bewersdorf, "Optical nanoscopy: from acquisition to analysis," Annu. Rev. Biomed. Eng. **14**(1), 231–254 (2012).
4. B. Huang, W. Wang, M. Bates, and X. Zhuang, "Three-Dimensional Super-Resolution Imaging by Stochastic Optical Reconstruction Microscopy," Science **319**(5864), 810–813 (2008).
5. I. Izeddin, M. El Beheiry, J. Andilla, D. Ciepielewski, X. Darzacq, and M. Dahan, "PSF shaping using adaptive optics for three-dimensional single-molecule super-resolution imaging and tracking," Opt. Express **20**(5), 4957–4967 (2012).
6. B. C. Coles, S. E. Webb, N. Schwartz, D. J. Rolfe, M. Martin-Fernandez, and V. Lo Schiavo, "Characterisation of the effects of optical aberrations in single molecule techniques," Biomed. Opt. Express **7**(5), 1755–1767 (2016).
7. M. Schwertner, M. J. Booth, and T. Wilson, "Specimen-induced distortions in light microscopy," J. Microsc. **228**(1), 97–102 (2007).
8. D. S. Wan, M. Rajadhyaksha, and R. H. Webb, "Analysis of spherical aberration of a water immersion objective: application to specimens with refractive indices 1.33–1.40," J. Microsc. **197**(3), 274–284 (2000).
9. D. Burke, B. Patton, F. Huang, J. Bewersdorf, and M. J. Booth, "Adaptive optics correction of specimen-induced aberrations in single-molecule switching microscopy," Optica **2**(2), 177–185 (2015).
10. M. J. Mlodzianoski, M. F. Juette, G. L. Beane, and J. Bewersdorf, "Experimental characterization of 3D localization techniques for particle-tracking and super-resolution microscopy," Opt. Express **17**(10), 8264–8277 (2009).
11. Y. Li, Y. L. Wu, P. Hoess, M. Mund, and J. Ries, "Depth-dependent PSF calibration and aberration correction for 3D single-molecule localization," Biomed. Opt. Express **10**(6), 2708–2718 (2019).
12. R. McGorty, J. Schnitzbauer, W. Zhang, and B. Huang, "Correction of depth-dependent aberrations in 3D single-molecule localization and super-resolution microscopy," Opt. Lett. **39**(2), 275–278 (2014).
13. M. J. Mlodzianoski, P. J. Cheng-Hathaway, S. M. Bemiller, T. J. McCray, S. Liu, D. A. Miller, B. T. Lamb, G. E. Landreth, and F. Huang, "Active PSF shaping and adaptive optics enable volumetric localization microscopy through brain sections," Nat. Methods **15**(8), 583–586 (2018).
14. A. Edelstein, N. Amodaj, K. Hoover, R. Vale, and N. Stuurman, "Computer control of microscopes using microManager," *Current Protocols in Molecular Biology*, Frederick M. Ausubel, ed. (Wiley, 2010), Chapter 14.
15. M. J. Booth, M. A. A. Neil, R. Juškaitis, and T. Wilson, "Adaptive aberration correction in a confocal microscope," Proc. Natl. Acad. Sci. **99**(9), 5788–5792 (2002).
16. R. J. Noll, "Zernike Polynomials and Atmospheric-Turbulence," J. Opt. Soc. Am. **66**(3), 207–211 (1976).

Biomedical Optics EXPRESS

17. E. Hecht, *Optics*, 4th ed. (Addison-Wesley, Reading, Mass., 2002), pp. vi, 698 p.
18. R. P. Tas, C. Y. Chen, E. A. Katrukha, M. Vleugel, M. Kok, M. Dogterom, A. Akhmanova, and L. C. Kapitein, "Guided by Light: Optical Control of Microtubule Gliding Assays," Nano Lett. **18**(12), 7524–7528 (2018).
19. B. Huang, S. A. Jones, B. Brandenburg, and X. Zhuang, "Whole-cell 3D STORM reveals interactions between cellular structures with nanometer-scale resolution," Nat. Methods **5**(12), 1047–1052 (2008).
20. A. Chazeau, E. A. Katrukha, C. C. Hoogenraad, and L. C. Kapitein, "Studying neuronal microtubule organization and microtubule-associated proteins using single molecule localization microscopy," Methods Cell Biol. **131**, 127–149 (2016).
21. S. Stallinga and B. Rieger, "Accuracy of the gaussian point spread function model in 2D localization microscopy," Opt. Express **18**(24), 24461–24476 (2010).
22. M. Siemons, C. N. Hulleman, R. O. Thorsen, C. S. Smith, and S. Stallinga, "High precision wavefront control in point spread function engineering for single emitter localization," Opt. Express **26**(7), 8397–8416 (2018).
23. A. von Diezmann, M. Y. Lee, M. D. Lew, and W. E. Moerner, "Correcting field-dependent aberrations with nanoscale accuracy in three-dimensional single-molecule localization microscopy," Optica **2**(11), 985–993 (2015).
24. Y. Shechtman, S. J. Sahl, A. S. Backer, and W. E. Moerner, "Optimal Point Spread Function Design for 3D Imaging," Phys. Rev. Lett. **113**(13), 133902 (2014).
25. S. R. P. Pavani, M. A. Thompson, J. S. Biteen, S. J. Lord, N. Liu, R. J. Twieg, R. Piestun, and W. E. Moerner, "Three-dimensional, single-molecule fluorescence imaging beyond the diffraction limit by using a double-helix point spread function," Proc. Natl. Acad. Sci. U. S. A. **106**(9), 2995–2999 (2009).
26. M. F. Juette, T. J. Gould, M. D. Lessard, M. J. Mlodzianoski, B. S. Nagpure, B. T. Bennett, S. T. Hess, and J. Bewersdorf, "Three-dimensional sub-100 nm resolution fluorescence microscopy of thick samples," Nat. Methods **5**(6), 527–529 (2008).